










RESEARCH ARTICLE | JUNE 07 2024

# Ultrasensitive terahertz response mediated by split ring antenna induced giant resonant field enhancement

Jinhua Zhang ; Miao Cai ; Xingguo Zheng; Dangdang Li; Shuxiang Ma; Xuebao Li ; Jingjing Fu ; Yinghao Yuan; Lin Chen ; Xuguang Guo  ; Yiming Zhu  ; Songlin Zhuang



APL Photonics 9, 066105 (2024)

<https://doi.org/10.1063/5.0205333>



View  
Online



Export  
Citation

11 June 2024 08:01:24

**AIP Photonics**

Special Topic: Brillouin Scattering  
and Optomechanics

**Submit Today**

# Ultrasensitive terahertz response mediated by split ring antenna induced giant resonant field enhancement

Cite as: APL Photon. 9, 066105 (2024); doi: 10.1063/5.0205333

Submitted: 26 February 2024 • Accepted: 24 May 2024 •

Published Online: 7 June 2024



Jinhua Zhang,<sup>1</sup>  Miao Cai,<sup>1</sup>  Xingguo Zheng,<sup>2</sup> Dangdang Li,<sup>1</sup> Shuxiang Ma,<sup>1</sup> Xuebao Li,<sup>1</sup>  Jingjing Fu,<sup>1</sup>   
Yinghao Yuan,<sup>1</sup> Lin Chen,<sup>1</sup>  Xuguang Guo,<sup>1,a)</sup>  Yiming Zhu,<sup>1,3,a)</sup>  and Songlin Zhuang<sup>1</sup>

## AFFILIATIONS

<sup>1</sup> Shanghai Key Lab of Modern Optical Systems, Terahertz Technology Innovation Research Institute, and Engineering Research Center of Optical Instrument and System, Ministry of Education, University of Shanghai for Science and Technology, Shanghai 200093, China

<sup>2</sup> Laboratory of Thin Film Optics, Shanghai Institute of Optics and Fine Mechanics, Chinese Academy of Sciences, Shanghai 201800, China

<sup>3</sup> Shanghai Institute of Intelligent Science and Technology, Tongji University, Shanghai 200092, China

<sup>a)</sup> Authors to whom correspondence should be addressed: [xgguo@usst.edu.cn](mailto:xgguo@usst.edu.cn) and [ymzhu@usst.edu.cn](mailto:ymzhu@usst.edu.cn)

## ABSTRACT

Optical resonators are widely utilized to enhance light-matter interaction by focusing electromagnetic waves into deep sub-wavelength regions. Here, we first present a metallic bowtie split ring (BSR) optical resonator as an asymmetric light coupler for a terahertz (THz) graphene photothermoelectric (PTE) detector. The giant THz field enhancement in the slit region of BSR is mediated by two types of resonances: the inductor-capacitor (LC) and the dipole resonances, which greatly increase the THz absorption, resulting in the sensitivity improvement of the THz PTE detector. In detail, the LC and dipole resonant behaviors of BSR are systematically investigated in both theoretical and experimental aspects. Compared with the dipole resonance, the LC resonance leads to stronger electric field localization and enhancement. An optimized BSR is designed and integrated with a graphene THz PTE detector, and an ultrasensitive THz PTE response is demonstrated. At room temperature and in zero-bias mode, the key detection parameters—responsivity, sensitivity (noise-equivalent power), and speed—are 138 V/W, 25 pW/Hz<sup>1/2</sup>, and 3.7 μs, respectively. Our results indicate that the LC resonance supported by BSR can introduce strong local field enhancement, which is helpful for realizing high sensitivity THz detectors.

© 2024 Author(s). All article content, except where otherwise noted, is licensed under a Creative Commons Attribution (CC BY) license (<https://creativecommons.org/licenses/by/4.0/>). <https://doi.org/10.1063/5.0205333>

## I. INTRODUCTION

One of the key components in the development of terahertz (THz) applications is the detection of THz waves.<sup>1–12</sup> High-sensitivity and high-speed room temperature THz detectors are important for a variety of potential THz applications.<sup>13–16</sup> Due to the frequency-independent interband absorption and high intraband absorption in THz and infrared regimes, the hot carrier effect, and the high thermoelectric (Seebeck) coefficient,<sup>17,18</sup> graphene has become one of the best two-dimensional materials for the development of high-sensitivity,<sup>19–23</sup> zero-bias, and room-temperature photothermoelectric (PTE) detectors.<sup>24,25</sup> The PTE response can be

expressed as

$$V_{\text{PTE}} = - \int S \times \nabla T(x) dx, \quad (1)$$

where  $V_{\text{PTE}}$  is the PTE open-circuit voltage,  $T$  is the temperature, and  $S$  is the Seebeck coefficient. Equation (1) indicates that for a uniform distribution of Seebeck coefficients, asymmetric temperature gradients are required.<sup>26</sup> Asymmetric coupling antennas are a promising approach to realize THz field enhancement and the resultant asymmetric temperature gradient. In addition,

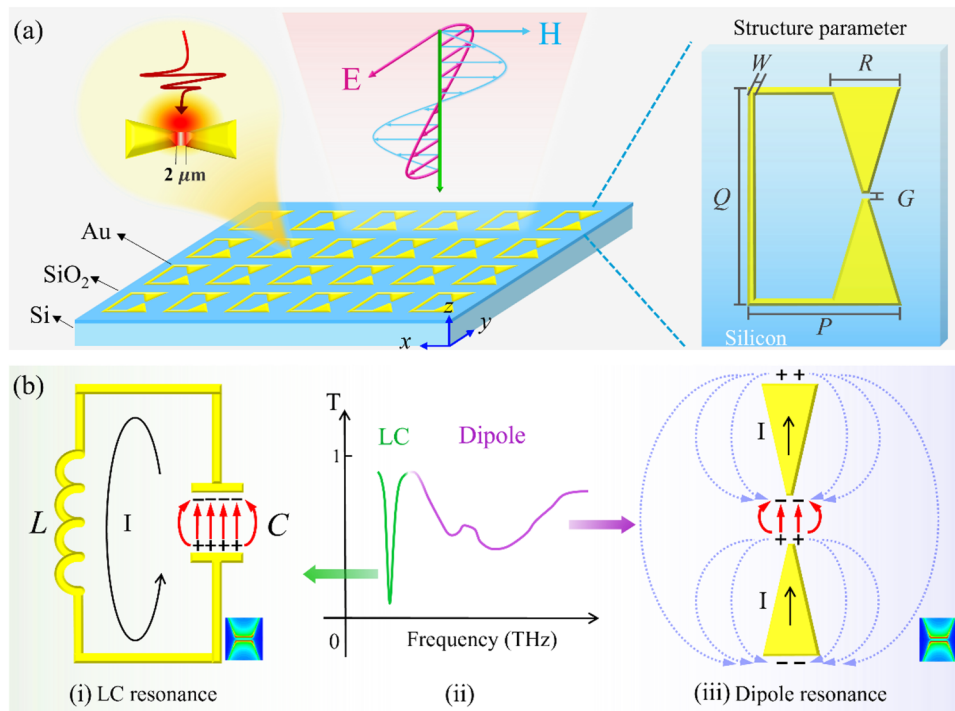


**FIG. 1.** Design principle and structural parameters of the BSR coupling structure. (a) The schematic diagram of a BSR excited by a THz wave and the structure parameters. (b) (i) LC and (ii) Dipole resonances.

the antenna-mediated THz field localization on the deep sub-wavelength graphene photoactive surface leads to the sensitivity improvement of THz detectors.

The dipole resonance of asymmetric antennas is widely used in THz PTE detectors.<sup>27–29</sup> In 2019, Castilla *et al.* proposed a THz detector containing a dipole antenna with a gap of 100 nm.<sup>30</sup> The antenna gap is used to concentrate the incident THz radiation and the antenna-induced local field to form a temperature gradient. Therefore, the centrosymmetric temperature gradient achieves a more sensitive PTE response. In 2021, Asgari *et al.* utilized the dipole resonance to enhance the electric field at the center of the antenna, and PTE can be activated in asymmetric mode under zero-bias operation. The NEP is on the order of 1 nW/Hz<sup>1/2</sup>.<sup>24</sup>

In comparison with the dipole resonance, the inductor–capacitor (LC) resonance supported by the split ring (SR) is rarely reported as a radiation coupling mechanism to improve the THz detection performance.<sup>31–38</sup> In general, the SR resonators support two types of resonances: LC (in a lower frequency region) and dipole (in a higher frequency region). If SR resonators are utilized as the asymmetric coupling antenna in THz detectors, different resonant modes can be excited under illumination of THz waves, which are expected to realize multiband response and greatly improve the performance of THz detectors.

In this work, we propose a bowtie SR (BSR) structure as the coupling antenna for THz PTE detectors. The resonant mechanisms of the BSR antenna are studied systematically. Based on an optimized BSR, a high-sensitivity graphene PTE THz detector

is demonstrated. First, the resonant behaviors of metallic periodic arrays composed of dipole antennas and BSR units (Fig. 1) are calculated numerically using a commercial FDTD electromagnetic simulation package (Lumerical Solutions).<sup>39</sup> We found that the BSR supports two resonant modes: the narrow low-frequency LC resonances and the broad high-frequency dipole resonances. In comparison with dipole antennas, BSR supports broader dipole resonances, but the different arm shapes have no essential effects on the LC resonances. When the LC and dipole resonances supported by the two structures are excited by the incident electromagnetic waves, there is field localization and enhancement in the sub-wavelength slit regions of the structures. The LC resonances introduce much stronger field enhancements. Second, the two periodic array structures were prepared by using standard semiconductor fabrication processes, and their transmission spectra were measured with a THz time-domain spectroscopy system (THz-TDS).<sup>40</sup> The experimental results agree well with the numerical simulation results; thus, the resonant characteristics of the two structures are verified. Finally, a room-temperature, zero-bias, and high-sensitivity graphene PTE THz detector is realized based on the optimized BSR structure. Due to the huge field enhancement mediated by the BSR structure, the THz detector shows superior detection performance.

## II. RESONANT PRINCIPLE AND STRUCTURE DESIGN

The proposed BSR resonator on an intrinsic silicon substrate is shown in Fig. 1(a). Such a structure can be prepared by using

ultraviolet photolithography, thin film deposition, and lift-off technology (Fig. S1 in the [supplementary material](#)). The structure parameters are as follows: the intrinsic silicon substrate thickness is  $500\ \mu\text{m}$ , the metal thickness of the BSR is  $50\ \text{nm}$  (Ti/Au, 10/40 nm), the length and width of the BSR are  $P = 63\ \mu\text{m}$  and  $Q = 90\ \mu\text{m}$ , respectively, the width of the bowtie is  $R = 29\ \mu\text{m}$ , the width of the other metal lines is  $W = 3\ \mu\text{m}$ , and the slit width of the bowtie is  $G = 2\ \mu\text{m}$ .

As the excitation source, the THz plane wave with the polarization parallel to the slit edges of the BSR generates currents in the structure, which induce two resonant modes, the low-frequency LC resonance and the high-frequency dipole resonance shown in Fig. 1(b), respectively. The LC and dipole resonances correspond to a circular oscillation current pattern around the BSR and a two-parallel-current pattern along the two arms of the structure in the  $y$  direction, respectively. At the resonant frequencies, the amplitudes of current reach their maximum values. A large amount of positive and negative charges accumulates at the two edges of the slit when the magnitude of the induced currents approaches zero, resulting in a strong electric field and then the electric-field energy localization in the slit region. On the contrary, when the induced currents reach their maximum values, the accumulated charges at the two edges of the slit disappear, and the electromagnetic field energy is stored as magnetic energy. The LC resonance supported by the BSR can be described by the LC equivalent circuit shown in Fig. 1(b-i), where the metal-line loop is equivalent to the inductor  $L$  and the slit is equivalent to the capacitor  $C$ . The relationship between the equivalent capacitance  $C$ , the equivalent inductance  $L$ , and the resonant frequency is as follows:<sup>41</sup>

$$f_{\text{LC}} = \frac{1}{2\pi\sqrt{LC}}. \quad (2)$$

The dipole resonance supported by the BSR can be described by two equivalent dipole antennas shown in Fig. 1(b-iii). The two metal arms along the  $y$  direction are equivalent to two dipole antennas. The parallel oscillation currents along the two edges of the ring in the  $y$  direction are excited at the dipole resonant frequency. The dipole resonant frequency is

$$f_{\text{dipole}} = \frac{\lambda}{n_{\text{eff}}} = \frac{c}{n_{\text{eff}}l}, \quad (3)$$

where  $c$  is the speed of light in a vacuum,  $n_{\text{eff}} = (n_{\text{si}} + 1)/2$  with  $n_{\text{si}} = 3.5$ , the refractive index of the intrinsic silicon substrate,<sup>42</sup> and  $l$  is the length of the dipole antenna.<sup>43</sup> It is very important to note that the distance between the two equivalent dipole antennas is only  $50\ \mu\text{m}$ , which is much smaller than the wavelength, so they have a near-field coupling.

### III. NUMERICAL SIMULATIONS AND EXPERIMENTAL MEASUREMENTS

We use the FDTD simulation to acquire the transmission spectra. As the excitation source, pulse plane waves are above the periodic arrays, the incident waves propagate along the  $z$  direction, and the electric field is parallel to the  $y$  direction. The Floquet periodic boundary conditions are adopted in the  $x$  and  $y$  directions. The perfectly matched layer absorption boundary conditions are used

in  $z$  directions to absorb the reflection and transmission waves in  $\pm z$  directions. Considering the trade-off between efficiency and precision, the mesh parameters are divided into two types: near the air-metal and dielectric-metal interfaces, the mesh is set to be a  $0.1\ \mu\text{m}$  cube; away from the metallic structure, the mesh is set to be a  $0.5\ \mu\text{m}$  cube. First, the transmission spectra of a dipole antenna [Fig. 2(a)], with a length of  $90\ \mu\text{m}$ , a width of  $3\ \mu\text{m}$ , a slit width of  $2\ \mu\text{m}$ , and periods of  $50\ \mu\text{m}$  in the  $x$  direction and  $180\ \mu\text{m}$  in the  $y$  direction, are simulated. The simulation results [Fig. 2(a)] show that the dipole array has a transmission dip at  $1.3\ \text{THz}$  and the transmittance is 16%. The spectral features originate from the dipole resonance; there is a parallel-current pattern along the dipole metal arms. The full width at half maximum (FWHM) of the resonant dip is about  $0.96\ \text{THz}$ . In addition, the length and width of the BSR [Fig. 2(b)] are  $63$  and  $90\ \mu\text{m}$ , where  $R$  has a width of  $29\ \mu\text{m}$ , and the periods in the  $x$  and  $y$  directions are  $100$  and  $180\ \mu\text{m}$ , respectively. A new dip with a FWHM of  $0.36\ \text{THz}$  and a transmittance of 32% appears in the transmission spectrum at  $0.2\ \text{THz}$ , which corresponds to the LC resonance and the current pattern oscillation as a circular. On the condition of polarization of the incident plane wave in the  $y$  direction, to clearly understand the dipole resonance, the BSR can be considered as two coupled dipole antennas along the  $y$  direction (without a slit for the left antenna and with a slit for the right one) that are connected by two metal arms. The dipole resonant behaviors are determined by the short-circuit dipole resonance of the left antenna, the open-circuit dipole resonance of the right antenna, and the coupling of the two antennas mediated by the near field and the two connection metal arms. Under the action of the bowtie, the dipole resonance of the BSR has a superior bandwidth. (The parametric scanning transmission spectra of the BSR are presented in Fig. S2 in the [supplementary material](#)). The simulation results show that the LC resonant frequency is determined solely by the structural parameters of the BSR and is not affected by the array periodicity. However, the dipole resonant frequency is determined by both the structural parameters of the unit cell and array periodicity. The comparative simulation results for the electric field being parallel to the  $x$  and  $y$  directions are shown in Fig. S3 in the [supplementary material](#).

According to the simulation results, we prepared the two structures shown in Fig. 2, the periodic dipole antenna and the BSR. In order to verify the simulation results, the transmission spectra of the two periodic arrays were measured using a home-made THz-TDS, and the results are shown in Figs. 2(a) and 2(b). The numerically simulated LC and dipole resonant frequencies for the two structures are in good agreement with the experimental results.

To better evaluate the light coupling performance of the two structures, light absorption as well as electric field localization and enhancement need to be further explored. Once the transmission and reflection spectra are numerically simulated, the absorption spectra can be derived numerically for the two structures [Fig. 3(a)]. Because the lossless substrate is set in our simulations, the absorption is due to the joule dissipation of metal structures, which is proportional to the square of the current. Therefore, at the LC and dipole resonant frequencies, the field-induced currents reach their maximum values, resulting in the absorption peaks at the resonant frequencies. As shown in Fig. 3(a), the blue curve represents the dipole resonance of the dipole antenna at  $1.33\ \text{THz}$ , and the absorbance at this resonance is 11%. The pink curves represent the absorption spectra of the BSR, in which there are two resonant

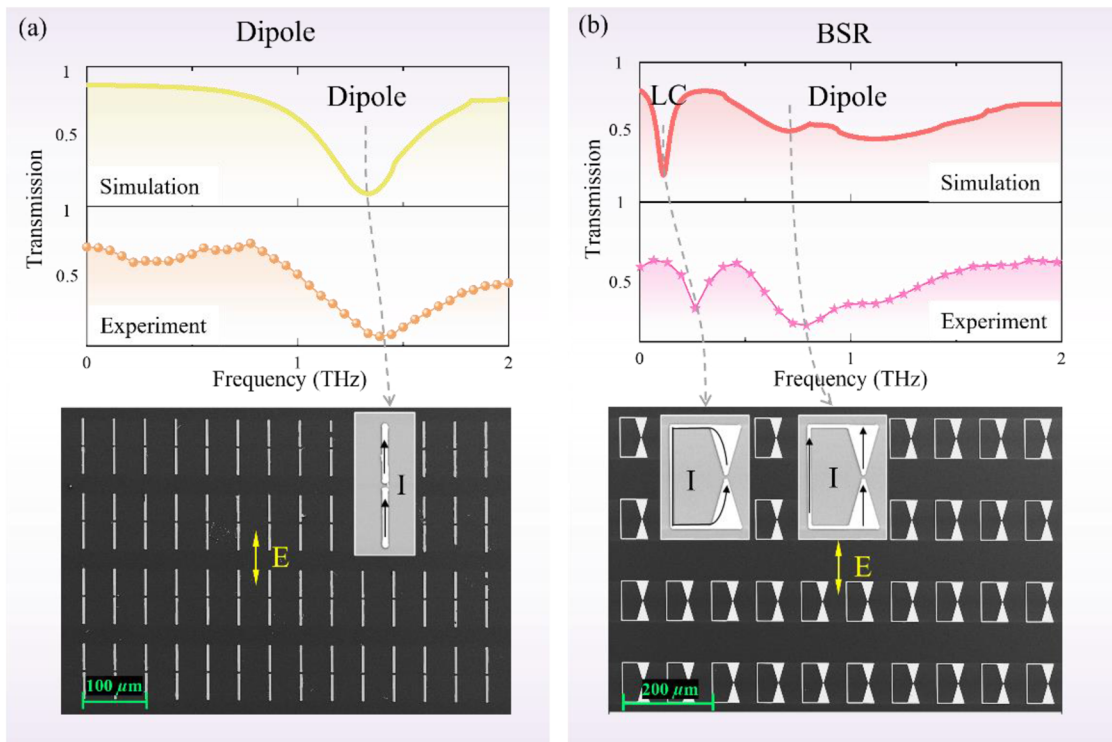


FIG. 2. (a) and (b) FDTD simulation results and experimental transmission spectra and the corresponding SEM images of dipole and BSR antenna arrays.

peaks (at 0.15 and 0.74 THz for the BSR), corresponding to the LC and dipole resonances, respectively. The absorbance of the LC and dipole resonances for the BSR is 20% and 3.5%, respectively. The electric field distributions at the LC (0.15 THz) and the dipole (0.74 THz) resonant frequencies of the BSR are shown in Figs. 3(b) and 3(c), respectively. Due to the accumulations of charge with different polarities at the two edges of the slit originating from the field-induced currents, there are strong open-circuit electric field enhancements in the deep sub-wavelength slit region of the BSR. Similar to the absorption spectra, the field enhancement at the LC resonant frequency is stronger than that at the dipole resonant frequency. If a graphene flake is put into the slit region, the strong oscillation electric field will induce free-electron abortion, resulting in the efficient transfer of electromagnetic energy into the electron system of graphene.

The electric field enhancements of the gap, defined as the ratio of surface-averaged electric field amplitudes with and without the metal structures as functions of frequency, are depicted in Fig. 3(d) for the two structures. The peak field enhancement frequencies for the dipole resonance of the dipole antenna and the LC resonances of the BSR are in agreement with the corresponding absorption peak frequencies shown in Fig. 3(a). However, because of the multi-origins of the dipole resonances of the BSR, there are some differences between the absorption and field enhancement spectra in the dipole resonant regions for the BSR. The numerical LC-resonant-induced field enhancement factors are larger than 50, corresponding

to field energy enhancements of more than three orders of magnitude. In a real situation, the various losses will introduce a reduction in field enhancement, but a strong field enhancement is expected to be realized in an experiment.

The current distribution patterns at the LC and dipole resonant absorption peaks of 0.15 and 0.74 THz [Fig. 3(a)] are shown in Figs. 3(e) and 3(f), respectively. It can be seen that at the LC resonant frequency, a toroidal pattern of current flow is formed, which is a typical characteristic of LC resonance. The current flow starts at one slit edge of the bowtie and ends at the other edge, resulting in the accumulation of charges with different polarities at the two edges and the electric field localization in the deep sub-wavelength slit region. The current distribution at the dipole resonant frequency is very different from that at the LC resonant frequency. Under the illumination of an electric field in the  $y$  direction, two parallel currents flowing toward the same direction are excited in the two arms along the  $y$  direction. In the right bowtie metal arm, an open-circuit resonance is formed with charges accumulated at the slit edges and the upper and lower boundaries of the metal arm. In the left metal arm, a short-circuit resonance is generated, and the charges accumulate at the upper and lower boundaries of the metal strip. Because of the difference between the two arms along the  $y$  direction, the charge numbers accumulated at the two upper boundaries and the two lower boundaries are not the same, which leads to current flows with different polarities in the metal arms along the  $x$  direction [Fig. 3(f)]. According to the intensity of electric field distributions [Figs. 3(b)

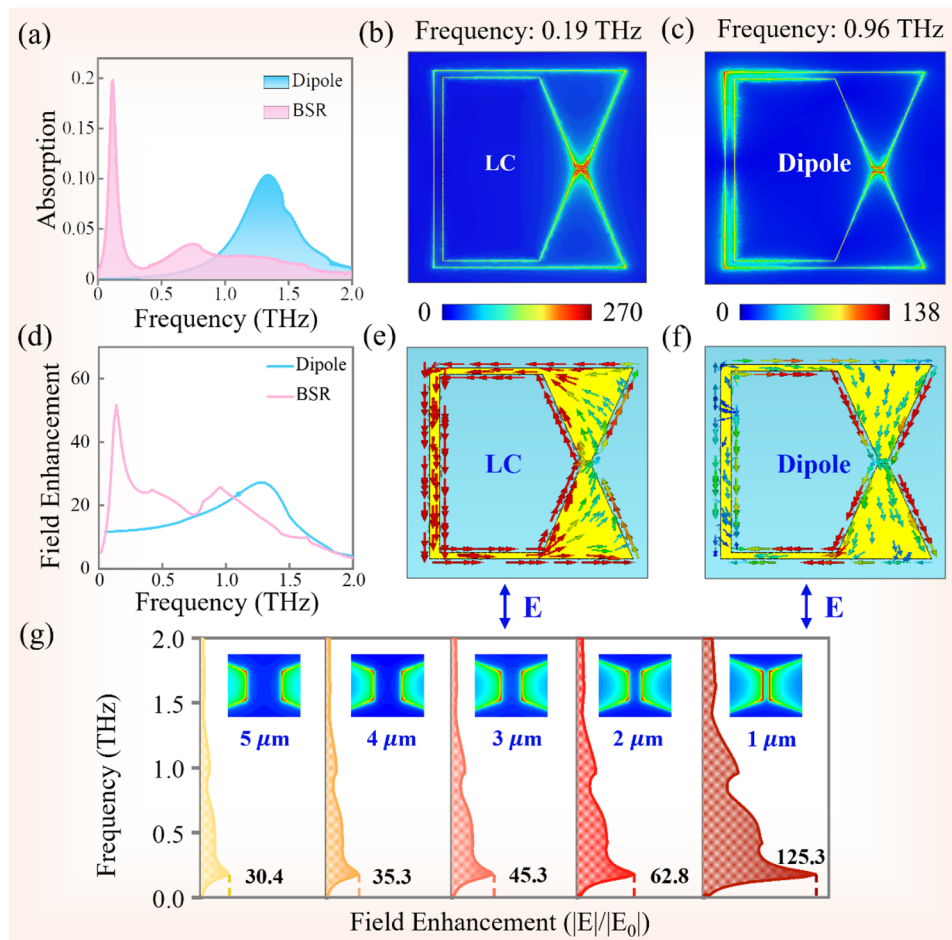


**FIG. 3.** (a) The numerical absorption spectra for the two structures, the simulated electric field distributions of the BSR at the LC (b) and dipole (c) resonant frequencies, (d) the surface-averaged electric field intensities in the slit regions of dipole and BSR with respect to frequency, the simulated current patterns of the BSR at the LC (e) and dipole (f) resonant frequencies, and (g) the surface-averaged and frequency-dependent electric field intensities of the BSR in the slit regions with different slit widths.

and 3(c)] and the electric field enhancement spectra [Fig. 3(d)], the electric field localization and enhancement ability of the BSR in LC resonant mode is greater than that in dipole resonant mode.

The effects of the slit width of the BSR on the electric field enhancement are numerically investigated. It can be seen from the capacitance expression of two parallel plates that the capacitance is inversely proportional to the distance between the two plates. The smaller distance between the two plates results in a larger capacitance. Therefore, the smaller width of the slit of the BSR leads to a larger averaged electric field in the slit. The surface-averaged electric field enhancement spectra are shown in Fig. 3(g) for the slit widths  $G = 1, 2, 3, 4,$  and  $5 \mu\text{m}$ , respectively. It can be seen that the LC resonance and dipole resonance are both affected by the slit width, and the surface-averaged electric field enhancement of the LC resonance increases much faster as the slit width decreases. For  $G = 1 \mu\text{m}$ , the surface-averaged electric field enhancement factor reaches up to 125.3. Therefore, reducing the slit width is an effective way to improve the electric field enhancement. Previous reports

show that when the slit width reaches the nanometer level, the field enhancement increases exponentially.<sup>44–46</sup>

#### IV. GRAPHENE TERAHERTZ DETECTOR INTEGRATED WITH A BOWTIE SPLIT RING AS THE COUPLING ANTENNA

The two resonant modes, the narrow LC and the wide dipole resonance, supported by a BSR, can be utilized as the asymmetric coupling antenna to localize the electromagnetic energy on the photoactive area of a detector. Here, we first used BSR as the asymmetric coupling antenna to prepare a graphene PTE THz detector. Considering the strong intraband absorption and hot carrier characteristics of graphene in the 0.1 THz region, the LC resonant frequency of the BSR and then the peak response frequency are designed at around 0.1 THz. The structural parameters of the BSR are as follows: the length and width of the BSR are  $P = 97.5 \mu\text{m}$  and  $Q = 150 \mu\text{m}$ , respectively; the width of the bowtie is  $R = 50 \mu\text{m}$ ; the width of

the other metal lines is  $W = 5 \mu\text{m}$ ; and the slit of the bowtie is  $G = 3 \mu\text{m}$ . The FDTD simulations (Fig. S5 in the [supplementary material](#)) show that the LC resonant frequency of the BSR is not affected by the array periodicity, which indicates the LC resonant frequency is completely determined by the BSR structural parameters. For low frequency terahertz waves ( $<1.0 \text{ THz}$ ), the Au film is nearly lossless (perfect metal). In this case, the electric-field enhancement is weakly dependent on the resonant frequency.

The schematic diagram and optical microscopic image of the prepared graphene PTE THz detector are shown in Fig. 4(a). The thickness of the mechanically exfoliated multilayer graphene is about 4.5 nm (about 30 layers). We assume that the multilayer graphene flake is turbostratically stacked.<sup>47</sup> Thus, the Dirac-cone band-structure is preserved, and the electrical and thermal conductivities, absorption efficiency, and heat capacity are proportional to the layer number. The graphene flake is transferred onto the channel region of a pre-deposited metallic pattern (a BSR and an electrode) on the  $\text{SiO}_2/\text{Si}$  (300 nm/500  $\mu\text{m}$ ) substrate by using a “PDMS transfer” technique (Fig. S1 in the [supplementary material](#)). It is important to note that the transferred graphene flake is only in contact with one edge of the BSR slit to maintain the LC resonance. If the slit is covered by the conductive graphene flake, the equivalent capacitor will be destroyed, resulting in the disappearance of the LC resonance (Fig. S4 in the [supplementary material](#)). When a graphene flake is inserted into the BSR slit, the electrons in graphene will be driven by the time-harmonic oscillating electric field, and the electrons will be thermalized via electron–electron scattering. For evaluating the electron temperature distribution along the graphene channel, a two-temperature model was built. The details of the model are presented in Sec. 6 of the [supplementary material](#). The numerical results (Fig. S6, [supplementary material](#)) show that a strong asymmetric electron temperature distribution is formed,

resulting in a high PTE response. Finally, the graphene device is wired with metallic pins and mounted onto a PCB board for subsequent electrical and optical measurements. All the measurements are performed at room temperature.

To verify the photoresponse performance of the graphene detector, we performed the electrical and optical measurements (the measurement setup is shown in Fig. S7 in the [supplementary material](#)). First, we measured the current–voltage (I–V) curves of the graphene detector in dark and illumination (84-GHz continuous THz wave, linear polarization along the  $y$  direction) conditions, and the results are presented in Fig. 4(b). The dark linear I–V curve (black line) indicates excellent Ohmic contacts between the graphene channel and the electrodes, which is important for obtaining excellent detection performances. A resistance of 764  $\Omega$  can be derived from the dark I–V curve. The linear I–V curve (yellow line) in Fig. 4(b), measured in the illumination condition, is parallel to that measured in the dark condition, which indicates that the short-circuit photocurrent is independent of the bias voltage. Such a bias-independent photoresponse strongly indicates that the PTE effect is the dominant detection mechanism in the graphene detector, and the PTE voltage of 2.35 mV can be derived from the I–V photoresponse curve. To characterize the spectral response of the graphene device, we used the lock-in technique to measure the photocurrent response signal of the detector by using a solid-state THz wave source electrically modulated by a 1-kHz square wave signal. Figure 4(c) shows the zero-bias photocurrent response of the graphene detector with the linear polarization THz waves in  $x$  polarization and  $y$  polarization, respectively. When the detector is irradiated by a  $y$ -polarized THz wave, the photocurrent of the detector shows a response peak at 84 GHz, which can be interpreted as an enhanced response due to the LC resonance. The measured peak photoresponse frequency of the detector is not completely consistent

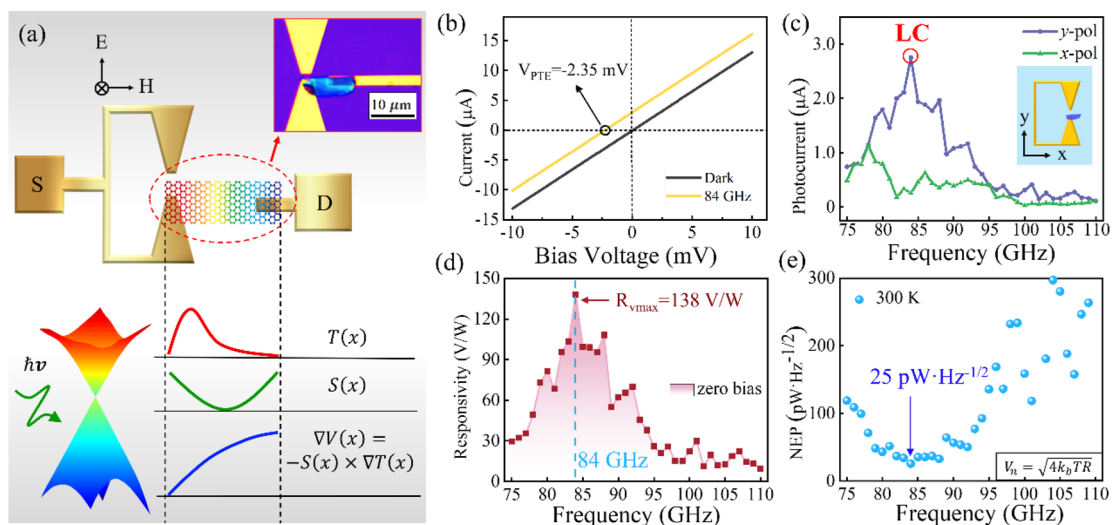


**FIG. 4.** Structure, principle, and measurement (at room temperature) results of the graphene PTE THz detector integrated with a BSR as the coupling antenna. (a) Schematic diagram, optical microscopic image, and PTE principle of the device. (b) Current–voltage (I–V) curve of the device under dark conditions and 84-GHz THz wave illumination. (c) Zero-bias photocurrents of the device when the polarizations of the incident THz wave are along the  $y$  and  $x$  directions, respectively. (d) Zero-bias responsivity of the device with the polarization of the incident THz wave along the  $y$  direction. (e) The noise-equivalent power (NEP) spectrum.

**TABLE I.** THz detectors based on 2D materials.

Mechanism	Material	Frequency	Responsivity	NEP	Response time	References
PTE	Graphene	84 GHz	138 V/W	25 pW/Hz <sup>1/2</sup>	3.7 μs	This work
PTE	Graphene	1 THz	10 V/W	1100 pW/Hz <sup>1/2</sup>	...	52
PTE	Graphene	2.52 THz	105 V/W	80 pW/Hz <sup>1/2</sup>	30 ns	30
Plasma wave	Graphene	0.31 THz	20 V/W	600 pW/Hz <sup>1/2</sup>	...	53
Bolometer	CNT	2.52 THz	0.54 A/W	...	200 μs	54
Photoconduction	BP	0.15 THz	300 V/W	1000 pW/Hz <sup>1/2</sup>	4 μs	55

with the designed LC resonant frequency, which can be explained by the capacitance change induced by the graphene flake partial filling of the slit and the influence of peripheral readout electrodes. When the detector is irradiated by an  $x$ -polarized THz wave, the photocurrent response of the detector is significantly weaker than that of the  $y$ -polarized THz wave, which is consistent with the previous analysis that the photoresponse peak at 84 GHz originates from the LC-resonance-mediated field local enhancement. Responsivity is a key parameter to estimate the performance of a THz detector. In this work, voltage responsivity ( $R_v$ ) is used, which is defined by the formula:  $R_v = V_{ph}/P_{in} \times S_a$ , where  $V_{ph}$  is the photovoltaic signal of the detector,  $P_{in}$  is the power density of the source (1.0 mW/cm<sup>2</sup>), and  $S_a$  is the effective photoactive area of the detector ( $S_a \approx 3\lambda^2/8\pi$ ).<sup>48</sup> As shown in Fig. 4(d), the peak responsivity of a graphene detector can reach up to 138 V/W at 84 GHz when the THz wave is  $y$ -polarized. In practical applications, noise equivalent power (NEP) is used to evaluate the sensitivity of detectors, which is calculated as the ratio between noise voltage and voltage responsivity ( $V_n/R_v$ ). For our graphene detectors, no external bias is required, the dominant noise is the Johnson–Nyquist white noise,<sup>49–51</sup> and the corresponding noise spectral density can be estimated by the formula  $V_n = \sqrt{4k_b TR}$ , where  $k_b$  is the Boltzmann's constant,  $T$  is the operating temperature (300 K), and  $R$  is the resistance of the detector (764 Ω). Figure 4(e) shows the NEP spectrum of the graphene detector. It can be seen that the NEP of the graphene detector can reach 25 pW/Hz<sup>1/2</sup> at the peak response frequency, showing excellent room temperature detection sensitivity. The detection parameters of the device were measured several times, and the experimental data were reproducible. To avoid the adsorption of impurities on the graphene channel, the device was kept in a vacuum chamber during the time interval between the two measurements. A detailed comparison of the detection performance of THz detectors is shown in Table I.

## V. CONCLUSIONS

In this work, a dual resonant BSR THz coupling antenna is proposed and implemented, which effectively enhances the PTE response of graphene THz detectors at zero bias and room temperature. This BSR structure has great potential applications in high sensitivity THz detection and THz sensing. First, the BSR optical coupling structure was systematically studied in both theoretical and experimental aspects. The transmission spectra measured by a THz-TDS are in good agreement with the simulation results, which verified the local enhancement of the THz field by the LC and dipole

resonances. Moreover, we find that the surface-averaged field intensity at the LC resonant frequency is stronger than that at the dipole resonant frequency. Subsequently, we demonstrate a PTE graphene THz detector integrated with a BSR coupling antenna. The excellent PTE response at room temperature indicates that the local field enhancement induced by the LC resonance plays a very key role. It is expected that an optimized single BSR antenna can be used as an efficient coupler for a THz PTE detector when the detection frequency is lower than 1.0 THz. Our results show that the electric field localization and enhancement mediated by the LC resonance is an important way to improve the performance of a PTE THz detector using two-dimensional materials such as graphene and other semimetals.

## SUPPLEMENTARY MATERIAL

See the [supplementary material](#) for more details on the fabrication process of the detector, the terahertz photoresponse measurement diagram, and the BSR FDTD simulations.

## ACKNOWLEDGMENTS

The authors gratefully acknowledge the National Natural Science Foundation of China (Grant Nos. 61988102, 62201349, and 61731020), the 111 Project (No. D18014), the Key Project supported by Science and Technology Commission Shanghai Municipality (Grant No. YDZX20193100004960), and the General Administration of Customs Project (No. 2020hk251).

## AUTHOR DECLARATIONS

### Conflict of Interest

The authors have no conflicts to disclose.

### Author Contributions

J.Z. and M.C. contributed equally to this work.

**Jinhua Zhang:** Conceptualization (equal); Data curation (equal); Formal analysis (equal); Investigation (equal); Software (equal); Validation (equal); Visualization (equal); Writing – original draft (equal). **Miao Cai:** Conceptualization (equal); Data curation (equal); Formal analysis (equal); Investigation (equal); Validation (equal); Visualization (equal); Writing – original draft (equal). **Xingguo Zheng:** Formal analysis (equal); Methodology (equal). **Dangdang Li:** Formal analysis (equal); Methodology (equal). **Shuxiang Ma:**



Formal analysis (equal); Methodology (equal). **Xuebao Li**: Formal analysis (equal); Methodology (equal). **Jingjing Fu**: Funding acquisition (equal); Methodology (equal). **Yinghao Yuan**: Formal analysis (equal); Methodology (equal). **Lin Chen**: Formal analysis (equal); Methodology (equal). **Xuguang Guo**: Formal analysis (lead); Funding acquisition (lead); Investigation (lead); Methodology (lead); Resources (lead); Writing – review & editing (lead). **Yiming Zhu**: Formal analysis (equal); Funding acquisition (equal); Investigation (equal); Methodology (equal); Resources (equal); Writing – review & editing (equal). **Songlin Zhuang**: Resources (equal); Supervision (equal).

## DATA AVAILABILITY

The data that support the findings of this study are available from the corresponding authors upon reasonable request.

## REFERENCES

- M. Tonouchi, “Cutting-edge terahertz technology,” *Nat. Photonics* **1**(2), 97–105 (2007).
- B. Ferguson and X.-C. Zhang, “Materials for terahertz science and technology,” *Nat. Mater.* **1**(1), 26–33 (2002).
- C.-H. Liu, Y.-C. Chang, T. B. Norris, and Z. Zhong, “Graphene photodetectors with ultra-broadband and high responsivity at room temperature,” *Nat. Nanotechnol.* **9**(4), 273–278 (2014).
- F. H. L. Koppens, T. Mueller, P. Avouris, A. C. Ferrari, M. S. Vitiello, and M. Polini, “Photodetectors based on graphene, other two-dimensional materials and hybrid systems,” *Nat. Nanotechnol.* **9**(10), 780–793 (2014).
- D. Akinwande, C. Huyghebaert, C.-H. Wang, M. I. Serna, S. Goossens, L.-J. Li, H.-S. P. Wong, and F. H. L. Koppens, “Graphene and two-dimensional materials for silicon technology,” *Nature* **573**(7775), 507–518 (2019).
- X. Zang, B. Yao, L. Chen, J. Xie, X. Guo, A. V. Balakin, A. P. Shkurinov, and S. Zhuang, “Metasurfaces for manipulating terahertz waves,” *Light: Adv. Mater.* **2**(2), 148–172 (2021).
- Y. Zhu, X. Zang, H. Chi, Y. Zhou, Y. Zhu, and S. Zhuang, “Metasurfaces designed by a bidirectional deep neural network and iterative algorithm for generating quantitative field distributions,” *Light: Adv. Manuf.* **4**(2), 104 (2023).
- C. Belacel, Y. Todorov, S. Barbieri, D. Gacemi, I. Favero, and C. Sirtori, “Optomechanical terahertz detection with single meta-atom resonator,” *Nat. Commun.* **8**(1), 1578 (2017).
- X. He, N. Fujimura, J. M. Lloyd, K. J. Erickson, A. A. Talin, Q. Zhang, W. Gao, Q. Jiang, Y. Kawano, R. H. Hauge, F. Léonard, and J. Kono, “Carbon nanotube terahertz detector,” *Nano Lett.* **14**(7), 3953–3958 (2014).
- Y. Peng, J. Huang, J. Luo, Z. Yang, L. Wang, X. Wu, X. Zang, C. Yu, M. Gu, Q. Hu, X. Zhang, Y. Zhu, and S. Zhuang, “Three-step one-way model in terahertz biomedical detection,” *PhotonIX* **2**(1), 12 (2021).
- J. Lyu, S. Shen, L. Chen, Y. Zhu, and S. Zhuang, “Frequency selective fingerprint sensor: The terahertz unity platform for broadband chiral enantiomers multiplexed signals and narrowband molecular AIT enhancement,” *PhotonIX* **4**(1), 28 (2023).
- L. Hong, L. Wang, M. Cai, Y. Yao, X. Guo, and Y. Zhu, “Sensitive room-temperature graphene photothermoelectric terahertz detector based on asymmetric antenna coupling structure,” *Sensors* **23**(6), 3249 (2023).
- T. Mueller, F. Xia, and P. Avouris, “Graphene photodetectors for high-speed optical communications,” *Nat. Photonics* **4**(5), 297–301 (2010).
- M. Ye, J. Zha, C. Tan, and K. B. Crozier, “Graphene-based mid-infrared photodetectors using metamaterials and related concepts,” *Appl. Phys. Rev.* **8**(3), 031303 (2021).
- F. Xia, T. Mueller, Y. Lin, A. Valdes-Garcia, and P. Avouris, “Ultrafast graphene photodetector,” *Nat. Nanotechnol.* **4**(12), 839–843 (2009).
- Y. Chen, Y. Wang, Z. Wang, Y. Gu, Y. Ye, X. Chai, J. Ye, Y. Chen, R. Xie, Y. Zhou, Z. Hu, Q. Li, L. Zhang, F. Wang, P. Wang, J. Miao, J. Wang, X. Chen, W. Lu, P. Zhou, and W. Hu, “Unipolar barrier photodetectors based on van der Waals heterostructures,” *Nat. Electron.* **4**(5), 357–363 (2021).
- X. Lu, L. Sun, P. Jiang, and X. Bao, “Progress of photodetectors based on the photothermoelectric effect,” *Adv. Mater.* **31**(50), 1902044 (2019).
- M. Dai, C. Wang, M. Ye, S. Zhu, S. Han, F. Sun, W. Chen, Y. Jin, Y. Chua, and Q. J. Wang, “High-performance, polarization-sensitive, long-wave infrared photodetection via photothermoelectric effect with asymmetric van der Waals contacts,” *ACS Nano* **16**(1), 295–305 (2022).
- N. M. Gabor, J. C. W. Song, Q. Ma, N. L. Nair, T. Taychatanapat, K. Watanabe, T. Taniguchi, L. S. Levitov, and P. Jarillo-Herrero, “Hot carrier–assisted intrinsic photoresponse in graphene,” *Science* **334**(6056), 648–652 (2011).
- J. C. W. Song, M. S. Rudner, C. M. Marcus, and L. S. Levitov, “Hot carrier transport and photocurrent response in graphene,” *Nano Lett.* **11**(11), 4688–4692 (2011).
- F. Bonaccorso, Z. Sun, T. Hasan, and A. C. Ferrari, “Graphene photonics and optoelectronics,” *Nat. Photonics* **4**(9), 611–622 (2010).
- J. Shi, Z. Li, D. K. Sang, Y. Xiang, J. Li, S. Zhang, and H. Zhang, “THz photonics in two dimensional materials and metamaterials: Properties, devices and prospects,” *J. Mater. Chem. C* **6**(6), 1291–1306 (2018).
- A. Rogalski, M. Kopytko, and P. Martyniuk, “Two-dimensional infrared and terahertz detectors: Outlook and status,” *Appl. Phys. Rev.* **6**(2), 021316 (2019).
- M. Asgari, E. Riccardi, O. Balci, D. De Fazio, S. M. Shinde, J. Zhang, S. Mignuzzi, F. H. L. Koppens, A. C. Ferrari, L. Viti, and M. S. Vitiello, “Chip-scalable, room-temperature, zero-bias, graphene-based terahertz detectors with nanosecond response time,” *ACS Nano* **15**(11), 17966–17976 (2021).
- Q. Qiu and Z. Huang, “Photodetectors of 2D materials from ultraviolet to terahertz waves,” *Adv. Mater.* **33**(15), 2008126 (2021).
- M. Dai, X. Zhang, and Q. J. Wang, “2D materials for photothermoelectric detectors: Mechanisms, materials, and devices,” *Adv. Funct. Mater.* **34**(21), 2312872 (2024).
- X. Chen and W. Fan, “Study of the interaction between graphene and planar terahertz metamaterial with toroidal dipolar resonance,” *Opt. Lett.* **42**(10), 2034 (2017).
- L. Luo, I. Chatzakis, J. Wang, F. B. P. Niesler, M. Wegener, T. Koschny, and C. M. Soukoulis, “Broadband terahertz generation from metamaterials,” *Nat. Commun.* **5**(1), 3055 (2014).
- X. Chen and W. Fan, “Ultra-high-Q toroidal dipole resonance in all-dielectric metamaterials for terahertz sensing,” *Opt. Lett.* **44**(23), 5876 (2019).
- S. Castilla, B. Terrés, M. Autore, L. Viti, J. Li, A. Y. Nikitin, I. Vangelidis, K. Watanabe, T. Taniguchi, E. Lidorikis, M. S. Vitiello, R. Hillenbrand, K.-J. Tielrooij, and F. H. L. Koppens, “Fast and sensitive terahertz detection using an antenna-integrated graphene pn junction,” *Nano Lett.* **19**(5), 2765–2773 (2019).
- M. Jeannin, G. Mariotti Nesurini, S. Suffit, D. Gacemi, A. Vasanelli, L. Li, A. G. Davies, E. Linfield, C. Sirtori, and Y. Todorov, “Ultrastrong light–matter coupling in deeply subwavelength THz LC resonators,” *ACS Photonics* **6**(5), 1207–1215 (2019).
- H.-T. Chen, W. J. Padilla, J. M. O. Zide, A. C. Gossard, A. J. Taylor, and R. D. Averitt, “Active terahertz metamaterial devices,” *Nature* **444**(7119), 597–600 (2006).
- X. He, “Tunable terahertz graphene metamaterials,” *Carbon* **82**, 229–237 (2015).
- Q.-Y. Wen, H.-W. Zhang, Y.-S. Xie, Q.-H. Yang, and Y.-L. Liu, “Dual band terahertz metamaterial absorber: Design, fabrication, and characterization,” *Appl. Phys. Lett.* **95**(24), 241111 (2009).
- N. Kim, S. In, D. Lee, J. Rhie, J. Jeong, D.-S. Kim, and N. Park, “Colossal terahertz field enhancement using split-ring resonators with a sub-10 nm gap,” *ACS Photonics* **5**(2), 278–283 (2018).
- H.-T. Chen, J. F. O’Hara, A. K. Azad, and A. J. Taylor, “Manipulation of terahertz radiation using metamaterials,” *Laser Photonics Rev.* **5**(4), 513–533 (2011).
- R. Singh, C. Rockstuhl, and W. Zhang, “Strong influence of packing density in terahertz metamaterials,” *Appl. Phys. Lett.* **97**(24), 241108 (2010).
- M. Dai, C. Wang, B. Qiang, Y. Jin, M. Ye, F. Wang, F. Sun, X. Zhang, Y. Luo, and Q. J. Wang, “Long-wave infrared photothermoelectric detectors with ultrahigh polarization sensitivity,” *Nat. Commun.* **14**(1), 3421 (2023).

- <sup>39</sup>J. Grant, I. Escorcía-Carranza, C. Li, I. J. H. McCrindle, J. Gough, and D. R. S. Cumming, “A monolithic resonant terahertz sensor element comprising a metamaterial absorber and micro-bolometer,” *Laser Photonics Rev.* **7**(6), 1043–1048 (2013).
- <sup>40</sup>W. Withayachumnankul and M. Naftaly, “Fundamentals of measurement in terahertz time-domain spectroscopy,” *J. Infrared, Millimeter, Terahertz Waves* **35**(8), 610–637 (2014).
- <sup>41</sup>S. Linden, C. Enkrich, M. Wegener, J. Zhou, T. Koschny, and C. M. Soukoulis, “Magnetic response of metamaterials at 100 terahertz,” *Science* **306**(5700), 1351–1353 (2004).
- <sup>42</sup>L. Novotny, “Effective wavelength scaling for optical antennas,” *Phys. Rev. Lett.* **98**(26), 266802 (2007).
- <sup>43</sup>A. Alù and N. Engheta, “Input impedance, nanocircuit loading, and radiation tuning of optical nanoantennas,” *Phys. Rev. Lett.* **101**(4), 043901 (2008).
- <sup>44</sup>Y.-M. Bahk, S. Han, J. Rhie, J. Park, H. Jeon, N. Park, and D.-S. Kim, “Ultimate terahertz field enhancement of single nanoslits,” *Phys. Rev. B* **95**(7), 075424 (2017).
- <sup>45</sup>M. A. Seo, H. R. Park, S. M. Koo, D. J. Park, J. H. Kang, O. K. Suwal, S. S. Choi, P. C. M. Planken, G. S. Park, N. K. Park, Q. H. Park, and D. S. Kim, “Terahertz field enhancement by a metallic nano slit operating beyond the skin-depth limit,” *Nat. Photonics* **3**(3), 152–156 (2009).
- <sup>46</sup>I. Romero, J. Aizpurua, G. W. Bryant, and F. J. G. de Abajo, “Plasmons in nearly touching metallic nanoparticles: Singular response in the limit of touching dimers,” *Opt. Express* **14**(21), 9988–9999 (2006).
- <sup>47</sup>R. Negishi, C. Wei, Y. Yao, Y. Ogawa, M. Akabori, Y. Kanai, K. Matsumoto, Y. Taniyasu, and Y. Kobayashi, “Turbostratic stacking effect in multilayer graphene on the electrical transport properties,” *Phys. Status Solidi B* **257**(2), 1900437 (2020).
- <sup>48</sup>D. Palaferri, Y. Todorov, A. Mottaghizadeh, G. Frucci, G. Biasiol, and C. Sirtori, “Ultra-subwavelength resonators for high temperature high performance quantum detectors,” *New J. Phys.* **18**(11), 113016 (2016).
- <sup>49</sup>N. Clément, K. Nishiguchi, A. Fujiwara, and D. Vuillaume, “One-by-one trap activation in silicon nanowire transistors,” *Nat. Commun.* **1**(1), 92 (2010).
- <sup>50</sup>A. A. Balandin, “Low-frequency  $1/f$  noise in graphene devices,” *Nat. Nanotechnol.* **8**(8), 549–555 (2013).
- <sup>51</sup>A. N. Pal and A. Ghosh, “Ultralow noise field-effect transistor from multilayer graphene,” *Appl. Phys. Lett.* **95**(8), 082105 (2009).
- <sup>52</sup>X. Cai, A. B. Sushkov, R. J. Suess, M. M. Jadidi, G. S. Jenkins, L. O. Nyakiti, R. L. Myers-Ward, S. Li, J. Yan, D. K. Gaskill, T. E. Murphy, H. D. Drew, and M. S. Fuhrer, “Sensitive room-temperature terahertz detection via the photothermoelectric effect in graphene,” *Nat. Nanotechnol.* **9**(10), 814–819 (2014).
- <sup>53</sup>D. A. Bandurin, I. Gayduchenko, Y. Cao, M. Moskotin, A. Principi, I. V. Grigorieva, G. Goltsman, G. Fedorov, and D. Svinsov, “Dual origin of room temperature sub-terahertz photoresponse in graphene field effect transistors,” *Appl. Phys. Lett.* **112**(14), 141101 (2018).
- <sup>54</sup>Y. Liu, Q. Hu, J. Yin, P. Wang, Y. Wang, J. Wen, Z. Dong, J.-L. Zhu, J. Wei, W. Ma, and J.-L. Sun, “Bolometric terahertz detection based on suspended carbon nanotube fibers,” *Appl. Phys. Express* **12**(9), 096505 (2019).
- <sup>55</sup>L. Wang, C. Liu, X. Chen, J. Zhou, W. Hu, X. Wang, J. Li, W. Tang, A. Yu, S.-W. Wang, and W. Lu, “Toward sensitive room-temperature broadband detection from infrared to terahertz with antenna-integrated black phosphorus photoconductor,” *Adv. Funct. Mater.* **27**(7), 1604414 (2017).